

Estimating the Urban Fractional Vegetation Cover Using an Object-Based Mixture Analysis Method and Sentinel-2 MSI Imagery

Yaotong Cai , Meng Zhang , and Hui Lin

Abstract—Accurate and efficient identification of the urban vegetation abundance is of great importance for urban planning and management. A lot of efforts have been made to estimate the urban fractional vegetation cover (FVC) using multispectral images by the pixel-based mixture analysis method. However, urban FVC maps comprising various meaningful landscapes have wider applications. Compared with other moderate spatial resolution multispectral imagery (e.g., SPOT, Landsat 8), the Sentinel-2 multispectral instrument (MSI) imagery has higher resolution, larger coverage, and shorter revisit time. So it may provide higher accuracy for urban FVC mapping. This article derives an accurate object-based urban FVC map for Changsha city, China, from the 10-m resolution Sentinel-2 data acquired in 2017. For producing the urban FVC maps, the mixture analysis methods were applied on segmental image objects instead of pixels. The results demonstrate that the object-based mixture analysis method achieved a higher FVC estimation accuracy than the pixel-based mixture analysis did, and it effectively removed the “salt and pepper” phenomena. The object-based linear model fully constrained least squares and achieved the best estimation accuracy ($R^2 = 0.92$, $RMSE = 0.0956$). The red-edge band reflectance information of the MSI imagery can improve the accuracy of the FVC maps, but not significantly. The object-based urban FVC maps would be a good alternative to the traditional pixel-based maps.

Index Terms—Fractional vegetation cover (FVC), object-based mixture analysis (OBMA), red edge band, Sentinel-2, urban.

I. INTRODUCTION

VEGETATION plays a significant role in nourishing human beings and keeping the sustainable development of the global environment [1], [2]. The urban vegetation is of great importance for urban sprawl modeling, air pollution mitigation, and urban heat island alleviation [3], [4]. The urbanization, however, decreases the fractional vegetation cover (FVC) quickly [5]–[7]. China has been advancing wide-scale urbanization in the recent three decades [8], [9]. In 2018, China has 147 cities with the population larger than 1 million and has 57.35% of the total

population living in cities [8]. Urban areas are facing decrease in FVC and environmental degradation [10]. Accurately and timely monitoring the change of vegetation abundance in urban areas at regional, national, and global scales is necessary for the healthy development of cities.

Remote sensing data have been widely used for urban FVC researches because of its wide coverage, easy accessibility, and short revisit period [11]–[19]. The aerial photography data, high spatial resolution imagery, and hyperspectral imagery can provide promising results, but they have poor spatial and temporal coverage [20]–[25]. The high price and complex processing procedure also impede their application in a global scale. The SAR data are immune to atmospheric conditions and have large temporal and spatial coverage. But when it is used for FVC estimation, the accuracy is low because of the strong penetration of radar signals [26], [27]. Multispectral data with moderate spatial resolutions, such as the Landsat imagery, have been used for FVC estimation [28]–[31]. The Landsat imagery has achieved good results in mapping the subpixel urban fractional cover. However, its relatively low spatial resolution may cause a spectrum mixture for estimating the FVC in heterogeneous urban areas [27], [29]. The Sentinel-2A satellites obtain multispectral instrument (MSI) images with higher spatial (10, 20, and 60 m) and spectral resolutions (13 bands) than that of Landsat [32]–[35], which can bring higher vegetation monitoring accuracy and FVC estimation accuracy. The red-edge band reflectance of the Sentinel-2 data, which is little sensitive to spectral noises, is closely connected with vegetation physiological parameters (nitrogen content, biomass), so it can be used to detect the health and pigment status of plants [36]–[38]. Therefore, Sentinel-2A MSI might be a good option for the FVC estimation.

A number of subpixel methods have been developed to estimate the FVC using the remote sensing data, including linear spectral mixture models (LSMM) and nonlinear spectral mixture models (NLSMM) [39]–[40]. LSMM includes the spectral mixture analysis (SMA) and the multiple endmember spectral mixture analysis (MESMA) [41]–[44]. In the scenarios with complex endmember spatial structures (vegetation and soil), multiple scattering is serious. In this case, the NLSMM (such as, probabilistic model, geometric-optical model, stochastic geometric model, and fuzzy model) can derive the endmember abundance more accurately than the LSMM [45]–[48]. However, the NLSMM contains cross-terminal endmembers, which may

Manuscript received July 3, 2019; revised September 17, 2019 and November 26, 2019; accepted December 23, 2019. Date of publication January 21, 2020; date of current version February 12, 2020. This work was supported in part by the National Natural Science Foundation of China under Grant 41901385 and in part by the China Postdoctoral Science Foundation under Grant 2019M652815. (Corresponding author: Meng Zhang.)

The authors are with the Central South University of Forestry and Technology, Changsha 410004, China (e-mail: yaotongcai@csuft.edu.cn; mengzhang@csuft.edu.cn; linhui@csuft.edu.cn).

Digital Object Identifier 10.1109/JSTARS.2019.2962550

cause collinearity and may have unmixing errors greater than that of the LSMM. Therefore, choosing an appropriate estimation model for FVC mapping in complex scenarios with mixed signals is important.

Usually, the estimation model is determined by the subpixel analysis, in which the spectral unmixing and FVC map generation are performed at the pixel level. Actually, the accurate vegetation information of a meaningful landscape or a defined geographic zone, which requires the FVC maps at the object level, is more useful to urban management [49], [50]. The object-based image analysis (OBIA) can reduce the influence of surrounding pixels and the “salt and pepper” phenomena by contexture procedures and integrating neighborhood information [51], [52]. Additionally, the OBIA can segment one image into objects of different scales, creating a layered set that is adaptable to different applications [53]. Therefore, the OBIA combined with the spectral unmixing analysis may be a better option for the urban FVC estimation than the pixel-based unmixing methods.

The advancement of global urbanization inevitably leads to the reduction and even disappearance of vegetation, affecting the regional and global climates and ecological environments. The urban FVC is usually estimated by the pixel-based mixture analysis using moderate spatial resolution images, such as EO-1/Hyprion and Landsat data. Medium–high resolution multispectral images (such as Sentinel-2) and the object-based mixture analysis (OBMA) method are seldom used. This article is to explore the performance of the OBMA method in estimating urban FVC using the Sentinel-2 MSI imagery. Both the LSMM and NLSMM models are used, as the urban areas are heterogeneous. The FVC maps are also derived from the Sentinel-2A data without red edge bands to analyze the influence of red edge bands on FVC estimation.

II. STUDY AREA AND DATA

A. Study Area

The study area is located in Changsha, latitudes $27^{\circ}51'$ to $28^{\circ}40'N$ and longitudes $111^{\circ}54'$ to $113^{\circ}15'E$, a city in the middle south of China. The city has a subtropical monsoon climate with four distinct seasons and very rich vegetation types. A 200 km^2 region in the downtown was selected as the study site. It has all typical urban land use/land cover types, such as residential areas, commercial areas, roads, parks, agriculture land, forests, water, and wetlands. The urban landscape is usually composed of vegetation, impervious land, and soil with different percentages in addition to water [54]. The study site is close to the Xiangjiang River, so there are streams, pools, and ponds. Therefore, a revised V (vegetation)-I (impervious surface)-S (soil)-W (water) model was applied in this study.

B. Remote Sensing Data and Processing

We used the clear (0% cloud cover) Sentinel-2A data (path/row: N0205_R075_T49RFM) acquired on September 15, 2017 from the European Space Agency website (<https://scihub.copernicus.eu/dhus/>) to estimate the FVC. The data have 13 bands, including visible, near-infrared, and short-wave bands.

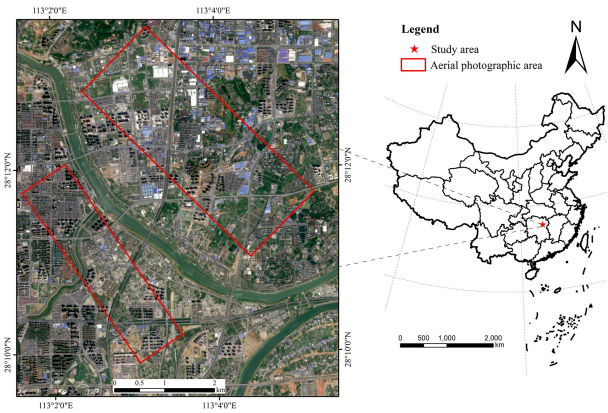


Fig. 1. Location of the study area and the aerial photographic areas. The study site is shown as a true color composite of the Sentinel-2 imagery (bands 4, 3, and 2 as red, green, and blue, respectively).

The five near infrared bands (four red edge bands and one NIR band) can be used for vegetation monitoring and analysis. Terrain correction and atmospheric correction were conducted to the Level-1C data using SRTM DEM and the Sen2Cor algorithm, respectively [55]. Moreover, 23 ground control points were selected to register the Sentinel-2A images. The 10- and 20-m resolution spectral bands were used in this study, and the 20-m bands were resampled to 10 m by the nearest neighbor interpolation.

The Landsat 8 OLI data (path/row: 123/40) obtained on September 12, 2017, which is close to the acquisition date of the Sentinel-2 images provided by the United States Geological Survey, were also used for FVC estimation. It has eight multispectral bands (resolution 30 m), one panchromatic band (resolution 15 m), and two thermal bands (resolution 100 m). Terrain correction, atmospheric correction, and geometric correction were also performed. Only the 30-m spatial resolution spectral bands (excluding coastal band) were selected for the FVC analysis.

The unmanned aerial vehicle (UAV) images (resolution 0.5 m) with three multispectral bands (red, green, and blue) collected on September 13, 2017 (no cloud cover) were employed to assess the accuracy of the FVC estimated from the above two data. Two aerial photographic areas (see Fig. 1) (0.8 and 1 km^2) were delimited and the flight missions were planned using a DJI Phantom 4 (DJI, Shenzhen, China). The images were automatically geotagged using the FEIMA UAV Manager during the flight and both the forward and side overlaps were set as 80%. Then Pix4DMapper was applied for image orthorectification and mosaicking.

The collected samples include streets trees, grassland, woodland, bare land, water body, road surface, and buildings. The FieldSpec Pro FR2500 back-mounted field hyperspectral radiometer from the Analytical Spectral Devices (ASD) company was used to collect the spectra of various materials, and a total of 90 samples of different surfaces were collected to establish reference spectral library. The spectra data were processed by dark calibration, wavelength calibration, radiometric calibration, and reflectance conversion.

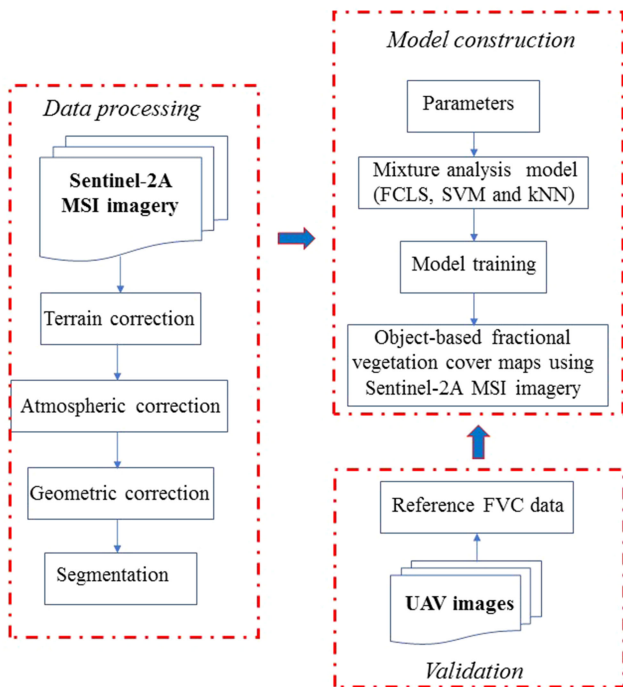


Fig. 2. Flowchart of the proposed method for urban FVC estimation.

We manually selected the regions of interest (ROI) according to the location of GPS points and Google Street View on the Sentinel-2 MSI image. Each component corresponds to an ROI of about 15–20 pixels. The spectra of these components were collected for establishing the image spectral library. All spectra of materials (including border tree, grass, forest, bare land, water body, road, and building measured by GPS) were converted using the band response function of Sentinel-2A to establish the image spectra library.

III. METHODOLOGY

We developed a method for urban FVC estimation using the Sentinel-2 MSI images and the OBMA method. The proposed method has four steps (see Fig. 2). First, generate the image objects by the multiresolution segmentation algorithm. Second, the endmember purification nonlinear SMA is used to identify “pure” objects. Subsequently, determine the spectra of each component using the image spectral library and the reference spectral library. Finally, the urban FVC maps are produced using the LSMM or NLSMM models.

A. Image Object Production

In this article, we used the multiresolution segmentation algorithm in eCognition Developer 9.0 (Trimble Germany GmbH, Munich, Germany) software [56] to produce image objects from the Sentinel-2 MSI [57]. The multiresolution segmentation algorithm constructs the primitive objects of different sizes using the heterogeneity threshold (1) and enhances the object generation response to the landscape patch structure. The heterogeneity threshold is a function of image layer weight, scale parameter,

shape (defines the weight of color when segmentation), and compactness. The scale parameter decides the object size, which influences the endmember selection in the subsequent steps. Considering the field observations and the spatial resolution of the images, segmentations used the scale parameters ranging between 1 and 30 pixels at an interval of 5 pixels for Sentinel-2 and between 1 and 12 pixels at an interval of 2 pixels for Landsat 8 to obtain an optimal scale parameter for creating objects and endmember selection

$$h_{\text{diff}} = \sum_c w_c (n_1 (h_{mc} - h_{1c}) + n_2 (h_{mc} - h_{2c})) \quad (1)$$

where h_{diff} is the regional heterogeneity, w_c represents the weight of the dimension, n_1 and n_2 are the area of different regions, h_{1c} and h_{2c} are the heterogeneity of two adjacent regions, and h_{mc} is the heterogeneity of the new merged region.

According to the visual examination and a series of tests, the scale parameters of 5 pixels (Sentinel-2) and 3 pixels (Landsat 8) were determined for endmember selection, and 50 pixels (Sentinel-2) and 15 pixels (Landsat 8) were set to generate objects. In addition, the hierarchical segmentation was performed to create objects at three levels using the scale parameter of 50, 100, and 150 pixels to investigate the advantage of OBMA in mapping FVC using the Sentinel-2 data. The shape and compactness required by the algorithm were kept as constants of 0.9 and 0.1.

B. Endmember Selection Based on Image Objects

Endmember selection is a key step in the SMA and high-quality FVC map generation. The endmember selection algorithms can be roughly divided into the endmember extraction algorithms (EEA) and the endmember generation algorithms (EGAs). EEA, including the pixel purity index [58], vertex component analysis, [59] and sequential maximum angle convex cone [60], assumes that there are pure pixels of different land cover types in the images, and all mixed pixels can be regarded as polyhedrons in the high-dimensional space, and the vertex of polyhedron is the endmember. EGA includes iterative error analysis [61], minimum volume transform [62], minimum volume constraint nonnegative matrix factorization [63], and endmember purification nonlinear SMA (EP-NSMA) [64]. EGA does not depend on the pure-pixel assumption and it directly generates the spectral features of “pure” endmembers. Although EEA can achieve promising results in some cases, the results of EGA are closer to actual conditions. Therefore, the EP-NSMA proposed by Ma *et al.* [64] was adopted to select the “pure” endmember in this study. The potential “pure” endmembers were selected by spectral purification of SMA, and then projected to the UAV imagery. Wrong endmembers (e.g., shadow pixels and edge pixels) were manually removed. The remained endmembers include vegetation (197), impervious surface (168), water (136), and soil (149).

Different from most research works that selected endmembers on the basis of pixels, this article extracted endmembers from the image objects, because a “pure” image object is more like a meaningful geographic unit, on the basis of which the noise,

TABLE I
PROPORTION OF FINAL LIBRARY FROM SENTINEL-2 OBJECTS AND ASD
HYPERSPETRAL IMAGERY

	Vegetation	Impervious surface	Soil	Water
ASD	9	6	2	2
Sentinel-2 Objects	3	2	1	0

shadow/shade, and complexity can be effectively reduced by the averaged value of the object. Furthermore, the spatial features of the image objects can improve the endmember selection, thereby reducing FVC estimation errors.

C. Spectral Library Construction for Each Biophysical Component

For the SMA, we produced a spectral library containing pure spectra of the components in the Sentinel-2 and hyperspectral imagery. The within-class spectral variability due to component degradation and exposure differences was considered in the spectra selection. Subsequently, count-based endmember selection (CoB) was applied to reduce the effect of interclass spectral ambiguity and intraclass redundancy [65]. The in_CoB and out_CoB values of each spectrum in the image spectral library and the reference spectral library were calculated. We compared the in_CoB and out_CoB values of the spectra of the corresponding components in the two spectral libraries (image spectral library and reference spectral library), and selected the spectra with higher in_CoB values and lower out_CoB values. The final spectral libraries for all biophysical components based on the selected spectral attributes of endmembers were established, which are the vegetation spectral library (12), impervious surface spectral library (8), soil spectral library (3), and water spectral library (2). The number of the image spectral library (Sentinel-2 objects) and the reference spectral library (ASD hyperspectral imagery) are shown in Table I.

D. Object-Based Mixture Analysis

On the basis of the segmented object images, three fixed endmember mixture analysis models were used for the mixture analysis, which are the least squares methods using fully constrained least squares (FCLS), support vector machine (SVM), and k-nearest neighbor (kNN). FCLS is an LSMM method, and SVM and kNN are NLSMM methods. We applied the radial basis function kernel (a nonlinear kernel) to run the SVM. For the Sentinel-2A images, the mixture analysis should be done twice, once with all the reference bands and once with the red-edge-band free reference bands to analyze the influence of red-edge on the FVC estimation. All the three algorithms were also employed to generate FVC maps from the Landsat 8 object images.

For comparison, the pixel-based mixture analysis methods were also used to generate FVC maps. Subsequently, the spectral library of each biophysical component was established using the approaches described in Sections III-B and -C. FCLS, SVM, and kNN were then employed to analyze each Sentinel-2A pixel and Landsat 8 pixel for producing the FVC maps.

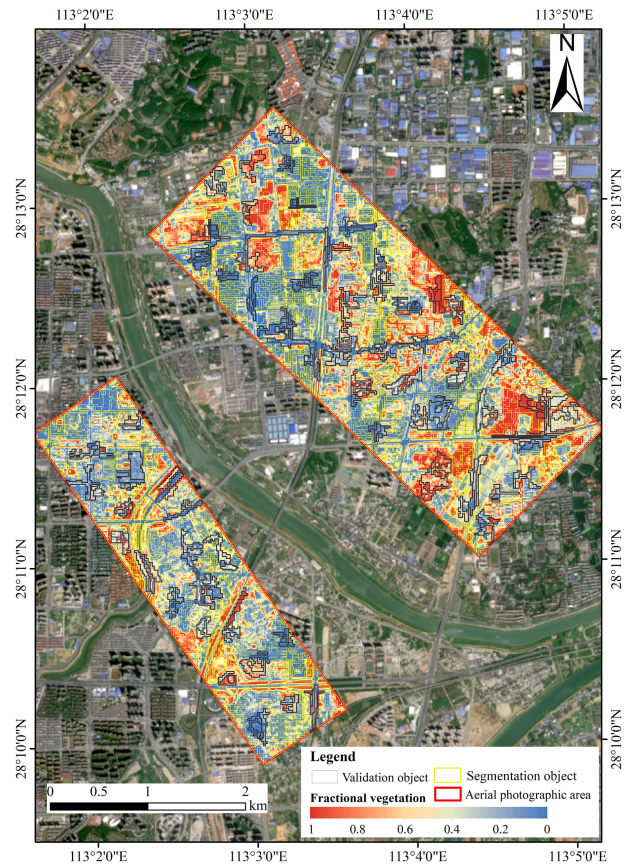


Fig. 3. Validation map.

In order to improve the FVC estimation accuracy, the shade normalization was used to account for the brightness differences between endmembers and image spectra. The nonshaded endmember component of each pixel was divided by the sum of all nonshaded endmember components, and finally the component of each pixel actually composing the endmember was obtained.

E. FVC Estimation Accuracy Assessment

For the accuracy assessment, the object-based FVC maps derived from Sentinel-2 and Landsat 8 images were compared with the manual interpretation results of the UAV images. We divided the 0.5-m resolution UAV images into 12 classes by the random forest algorithm (the classification map was validated by field data at the pixel level). These classes were then assigned to five components, which are vegetation, impervious surface, soil, water, and shadow. The labeled pixels were finally aggregated into the object level, and the fraction of vegetation within an object was generated. We only validated the vegetation fraction during the accuracy assessment. A total of 300 objects were randomly selected from the FVC maps generated from the Sentinel-2 imagery for the accuracy assessment (see Fig. 3). The sizes of the selected objects range from 5 to 8 pixels, and the mean and standard deviations are 6.4 and 1.2 pixels, respectively. Thus, the classification map generated from the UAV data could only be used as the reference data. For comparison, the pixel-based UAV classification maps were first aggregated using the

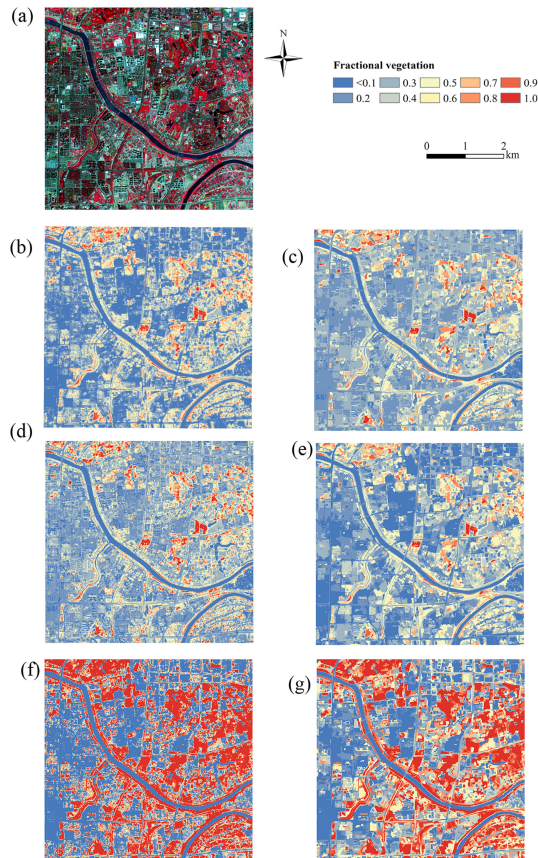


Fig. 4. (a) Standard false-color composite of the Sentinel-2 image. (b), (d), and (f) Pixel-based FVC maps obtained by FCLS, KNN, and SVM, respectively. (c), (e), and (g) Object-based FVC maps obtained by FCLS, KNN, and SVM, respectively.

selected validation image objects from the Sentinel-2 imagery. The coefficient of determination (R^2) and RMSE between the FVC maps generated from Sentinel-2A and Landsat 8 images was also calculated.

IV. RESULTS AND ANALYSIS

A. Object-Based and Pixel-Based FVC Maps Derived From Sentinel-2A

The FVC maps derived from Sentinel-2 by the OBMA methods with the scale parameter of 50 pixels were compared with the pixel-based FVC maps (see Fig. 4). The FVC maps obtained by FCLS (FVC-FCLS) and kNN (FVC-kNN) have similar spatial patterns of the vegetation component, which is close to that of the standard false composite of the Sentinel-2 image. Forest parks, cultivated land, and grassland have higher vegetation fractions than water body, bare land, and impervious surface (such as commercial areas, residential areas, and road) do. The vegetation fractions of the FVC maps obtained by SVM (FVC-SVM) are different. In the FVC-SVM maps, the vegetation fraction values of many areas are given extreme values of 0 or 1. Because of the maximum interval property of hyperplane, the SVM classifier is similar to the pixel dichotomy, which leads to over-classification. The vegetation fraction results in the object-based FVC-FCLS

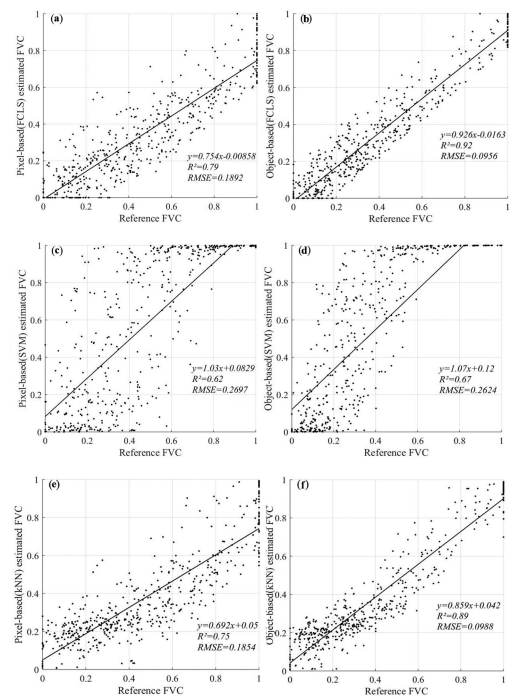


Fig. 5. Validation of the Sentinel-2 FVC maps using the reference data. (a), (c), and (e) Pixel-based FVC maps obtained by FCLS, SVM, and kNN, respectively. (b), (d), and (f) Object-based FVC maps obtained by FCLS, SVM, and kNN, respectively.

and FVC-kNN maps are shown by microlandscape units, which is similar to the actual situation. In the FVC maps obtained by OBMA, the vegetation fraction is presented at the object level, which is more useful for city managers. Furthermore, the “salt and pepper” phenomenon is more serious in the pixel-based FVC maps. The polarization of FVC maps has been attenuated in SVM when the OBMA method was used.

B. Accuracy of the FVC Maps

The accuracy of the FVC maps was assessed by the comparison with the reference data derived from the UAV images (see Fig. 5). For the object-based FVC maps [see Fig. 5(a)–(c)], the regression of Sentinel-2A and reference data yields a slope of near 1. The coefficient of determination (R^2) between the vegetation fraction in the object-based FVC maps and that in the reference data is larger than 0.67. Especially, the R^2 between the FVC-FCLS and the reference data and that between FVC-kNN and the reference data is above 0.89, indicating that the object-based vegetation fraction estimation methods are feasible in heavily urbanized areas. The linear model, FCLS, has the highest accuracy ($R^2 = 0.92$, $RMSE = 0.0956$), followed by nonlinear models kNN ($R^2 = 0.89$, $RMSE = 0.0988$) and SVM ($R^2 = 0.67$, $RMSE = 0.2624$). Validation results show that the pixel-based FVC estimation [see Fig. 5(d)–(f)] has smaller R^2 and larger RMSE than that of the object-based FVC estimation, suggesting that the object-based spectral unmixing method is more effective. FCLS also has the best performance in the pixel-based mixture analysis.

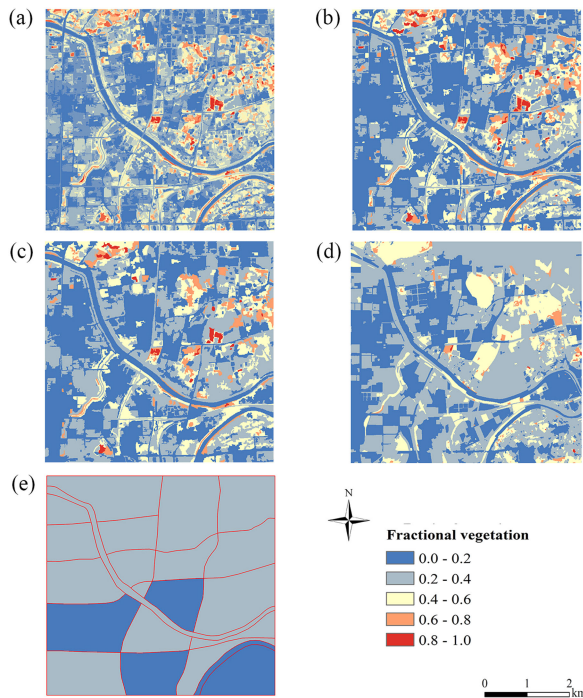


Fig. 6. Multiscale object-based FVC maps derived from Sentinel-2A images by FCLS with scales of (a) 50, (b) 100, and (c) 150. (d) FVC map for land use/land cover derived from the GF-2 images. (e) FVC map of the street district.

C. Multiscale FVC Maps

The OBMA method can generate multiple scale vegetation fraction maps adaptable to different applications. The object-based FCLS-FVC maps derived from the Sentinel-2 data with the scale parameters of 100, 150, and 150 pixels are shown in Fig. 6(a)–(c), respectively. The accuracy of these FVC maps is consistent with that of Fig. 5(a), because they were obtained by aggregating the OBMA results of the Sentinel-2A data with a scale parameter of 50 pixels. In the FVC maps of these three scales, the vegetation fraction shows a consistent pattern.

As the FVC map [see Fig. 6(d)] of land use/land cover derived from the GF-2 imagery (Fig. 7, Hunan Provincial Department of Natural Resources, 2017. <http://www.enhunan.gov.cn/>) shows, the lowest vegetation fraction (0–0.2) appears in the commercial areas. The residential areas also have very low vegetation fractions. Park forests, agriculture, and wetland areas have the largest vegetation coverage (0.8–1.0) [red color in Fig. 6(d)]. At the street district level, the vegetation fraction is 0–0.4 [see Fig. 6(e)], and the vegetation coverage of most of the street districts is between 0.2 and 0.4, which provides information for understanding the social and vegetation structures of urban neighborhoods.

D. FVC Maps Derived From the Landsat 8 OLI by the OBMA Method

To evaluate the robustness of the OBMA method, we also derived the FVC maps of the study area from the Landsat 8 OLI imagery (see Fig. 8). In the FVC-FCLS and FVC-kNN maps, the spatial patterns of the vegetation fractions are similar

Land cover type

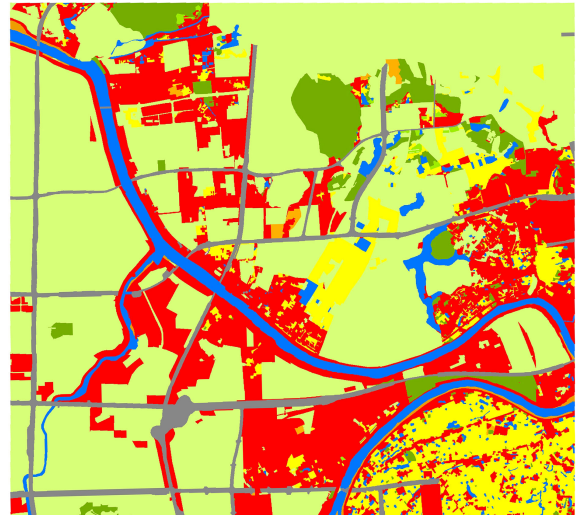
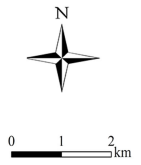
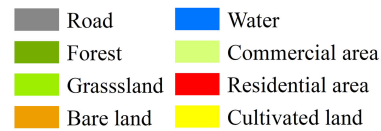


Fig. 7. Land use/land cover map.

to that of the standard false color composite imagery and the real condition. High vegetation fractions are distributed in or around forests, parks, and grassland. However, the result of FVC-SVM is seriously affected by polarization, so values 1 and 0 account for the majority of the map, the same as the results of the Sentinel-2A data. And the value 0 is dominating. This could be due to the low spatial resolution of Landsat8 OLI. The “salt and pepper” phenomenon is also more obvious in the pixel-based FVC maps, which is the same to the case of Sentinel-2A.

The determining coefficient (R^2), ranging from 0.56 to 0.84, was observed between the FVC results derived from the Landsat8 OLI image using OBMA and that from UAV images across all validation samples (see Fig. 9). Using the OBMA method, FCLS achieved R^2 of 0.84 and RMSE of 0.1163, which are better than the corresponding values of kNN ($R^2 = 0.67$, RMSE = 0.2559) and SVM ($R^2 = 0.56$, RMSE = 0.3215). The OBMA algorithms perform better than the pixel-based algorithms, reflecting the robustness of the OBMA method.

V. DISCUSSION

A. Influence of the Spectral Library on FVC Estimation Accuracy of Pixel-Based and Object-Based Methods

In this article, the final spectral library consists of the image spectral library and the reference library. In the image spectral library, the spectral of each component was derived from the average value of all endmembers in an object. Although the objects are relatively pure, endmember pixels have greater spectral variability than averaged objects, and a spectral library containing averaged endmembers may be unable to properly capture this variability. Therefore, we reprocessed the image spectral library

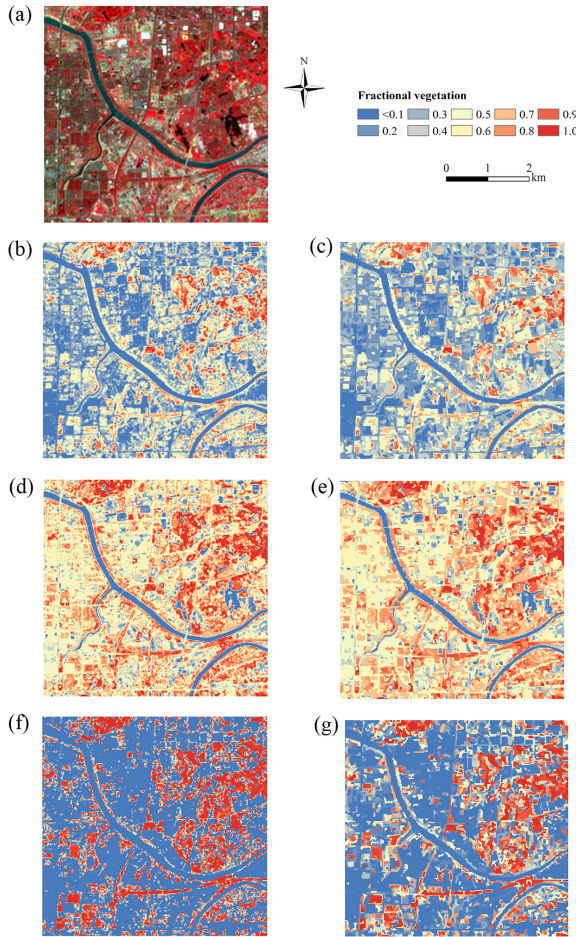


Fig. 8. (a) Standard false-color composite of the Landsat 8 image. (b), (d), and (f) Pixel-based FVC maps obtained by FCLS, KNN, and SVM, respectively. (c), (e), and (g) Object-based FVC maps obtained by FCLS, KNN, and SVM, respectively.

by selecting spectrum of the most representative endmember in the object as that of each component. The proportion of the reprocessed final library from the image spectral library and reference spectral library was the same as the previous library in Section III-C. The accuracies of the pixel-based and object-based methods are shown in Fig. 10. The outcome demonstrates that the accuracies of the FVC maps obtained by the pixel-based mixture analysis based on the spectral library in the pixel scale are higher than that based on the spectral library containing ASD spectra and object-extracted (averaged from the complete object) spectra. However, the results were exactly the opposite when we used the OBMA based on these two final spectral libraries. This indicates that the source of the library spectra can influence the accuracy of the pixel-based and OBMA method. In general, the object-based method performs better in estimating FVC in urban areas than the pixel-based method.

B. Merits and Demerits of the Proposed Method

SMA was often applied to obtain the vegetation abundance in urban areas from the hyperspectral imagery. Multispectral images have been gradually used to acquire FVC maps, thanks

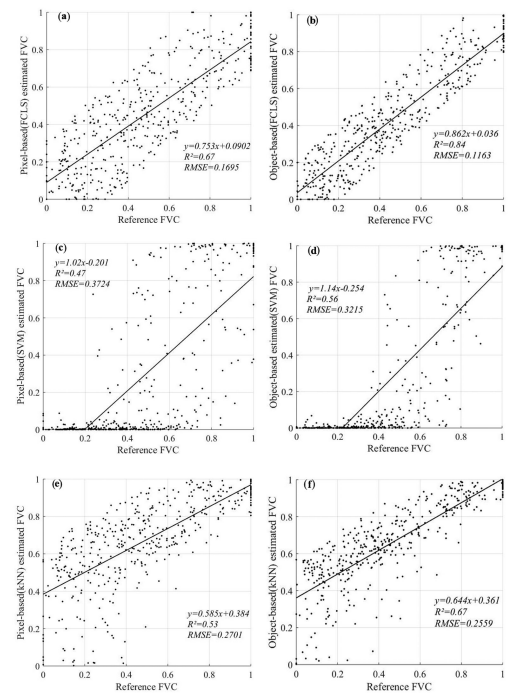


Fig. 9. Validation of the FVC maps derived from the Landsat8 OLI data using the reference data. (a), (c), and (e) Pixel-based FVC maps obtained by FCLS, SVM, and kNN, respectively. (b), (d), and (f) Object-based FVC maps obtained by FCLS, SVM, and kNN, respectively.

to its wide bandwidth, easy accessibility, and abundant band information. Although the pixel-based spectral mixture method has got a wider application than the OBMA algorithm, it cannot generate satisfying FVC maps in heterogeneous urban areas.

This study demonstrates that the OBMA method is more preferable for urban FVC estimation than the pixel-based one. First, the object-based FVC maps have higher accuracies than the pixel-based FVC maps. Second, the OBMA method can effectively remove the “salt and pepper” phenomena, which cannot be done by the pixel-based methods. In this article, the Sentinel-2 imagery was first segmented into objects, and then conducted a mixture analysis. Compared with the pixel-based mixture analysis method, the OBMA has three superiorities. First, capturing the precise outline of different objects at the pixel level is difficult, but describing a tree canopy, house, forest, and commercial district at the object level is possible. Objects obtained by the segmentation algorithm are homogeneous and can provide rich image features. Thus, they can eliminate the “salt and pepper” phenomenon and are more meaningful for describing geographic landscapes. Second, the OBMA method can generate FVC maps of different scales and geographic zones, which are adaptable to urban management and other applications. The results indicate that the OBMA method is robust, so it can be used to process other remote sensing data.

The proposed OBMA method has many advantages in urban FVC estimation, but it also subjects to some limitations. First the OBMA method involves the object-based endmember (OBE) selection. Similar to the pixel-based method, the OBE selection applies the trial and error procedure, which selects endmembers

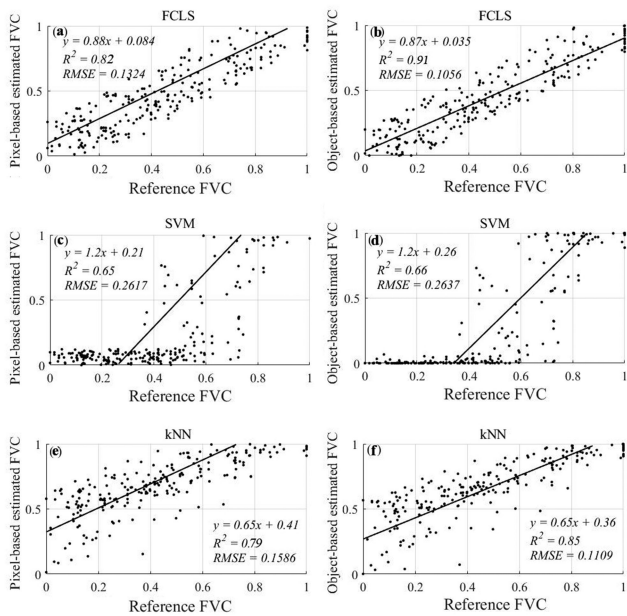


Fig. 10. Validation of the FVC maps derived from the Sentinel-2 data and reprocessed final spectral library using the reference data. (a), (c), and (e) Pixel-based FVC maps obtained by FCLS, SVM, and kNN, respectively. (b), (d), and (f) Object-based FVC maps obtained by FCLS, SVM, and kNN, respectively.

and computes the scores, then uses the threshold method to achieve an acceptable result. The OBMA method assumes that the selected OBE is “pure.” However, obtaining pure OBEs from the MSI imagery in urban areas is a challenge, and even more difficult from the medium spatial resolution (30 m) OLI imagery, as it depends on the segmentation scale parameter. Using a larger scale value in segmentation will generate heterogeneous objects, making it difficult to acquire pure OBE. Smaller scale values bring more homogeneous objects favorable for the OBE selection, but small endmember objects cannot depict the meaningful geographic unit [50]. Therefore, selecting a proper scale parameter for segmentation is essential for pure OBE identification. Arranging an object-based image spectral library combined with field survey data may be a way to solve this problem. Measuring the intrasegment homogeneity and the intersegment disparity could be another effective way to get the proper scale parameter. Second, the mixture analysis results of the object-based images are also affected by the scale parameters of segmentation. Theoretically, the mixture analysis can be applied to images of any scale segmentation. However, large-scale parameters in segmentation lead to low accuracies, and may produce a result with a small-scale value, which is similar to the case of the pixel-based method. Unmixing the image objects with an appropriate scale parameter, then aggregating vegetation abundance of larger objects from the former results may be a feasible way to solve this problem. Thus, the selection of scale parameters in segmentation is a decisive step of mixture analysis. Third, the mixture analysis methods (FCLS, SVM, and kNN) used in this study assume that the endmember number in a pixel is constant, so errors appear when the number and type of surface components change (e.g., heavily urbanized areas). Multiple

endmember mixture analyses, such as the multiple endmember SMA, allow the variation of endmembers for each pixel, so it may be a method to address those problems. Fourth, the FVC results derived from multispectral images by the OBMA are also subject to the spectral confusion of different surface components (e.g., shadow and water) in the heterogeneous urban areas. The spectral confusion will lead to collinearity, reducing the FVC estimation accuracy [66]. To address these issues, decorrelation or excluding endmember and image stratification have been introduced. Additionally, we validated the FVC map generated by the Sentinel-2 imagery at the object level. This may lead to some uncertainties because shadow/shade is not considered in the Sentinel-2 imagery, but it is clearly identified in the UAV classification map. The pixel-based Markov matrix can be used for the accuracy assessment of the FVC maps derived from the Sentinel-2 imagery in the future. The contribution of the band reflectance in Sentinel-2 data to the FVC estimation also needs further research.

For complex scenarios with mixed signals, choosing an appropriate mixture analysis model (linear or nonlinear) is significant. Among the LSMM (FCLS) and NLSMM (SVM and kNN) methods, FCLS achieved the highest FVC estimation accuracy in the urban environment. However, the model should be selected according to the nonlinearity degree of the mixed signals, which is the proportion of multiple scattering terms. If the multiple scattering is serious, the linear combination of endmembers cannot explain the nonlinear mixed signals, so NLSMM should be chosen [67]. If the three-dimensional structure of each endmember in an image is simple, the secondary collision of photons between different endmembers decreases, and the LSMM performs better [68]. Therefore, the quantitative analysis of the multiple scattering intensity in mixed pixels by field measurement or radiation transfer models and the analysis of factors affecting multiple scattering, such as area ratio, spatial distribution, and height difference of terminal elements, will be helpful to obtain the basis for model selection.

VI. CONCLUSION

This article proposed a “paradigm-shift” in deriving high resolution (10 m) vegetation abundance over urban areas from the Sentinel-2A MSI data (5-day) by the OBMA method. The experiments conducted in Changsha, China showed that the FVC estimation accuracy can be improved using the OBMA method. FCLS, an LSMM model, achieved the best estimation accuracy ($R^2 = 0.92$, $RMSE = 0.0956$). In general, the proposed method was effective and robust when it was applied to Sentinel-2A MSI, Landsat 8 OLI, and Sentinel-2A MSI data without red edge bands. The red edge band reflectance information in the MSI imagery can increase the accuracy of the FVC mapping products. The presented approach may be of significant importance for the urban vegetation monitoring, urban planning, and management.

ACKNOWLEDGMENT

The authors would like to thank the editors and anonymous reviewers for the valuable comments, which are significant for improving this article.

REFERENCES

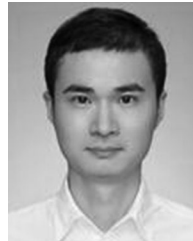
- [1] X. Mu, W. Song, Z. Gao, T. M. McVicar, and R. J. Donohue, "Fractional vegetation cover estimation by using multi-angle vegetation index," *Remote Sens. Environ.*, vol. 216, pp. 44–56, 2018.
- [2] Y. Yao, S. Liang, J. Cheng, Y. Lin, K. Jia, and M. Liu, "Impacts of deforestation and climate variability on terrestrial evapotranspiration in subarctic China," *Forests*, vol. 5, no. 10, pp. 2542–2560, 2014.
- [3] L. Nesitt and M. J. Meiner, "Exploring relationship between socioeconomic background and urban greenery in Portland, OR," *Forests*, vol. 7, no. 8, pp. 162–175, 2016.
- [4] J. Wang, Y. Li, J. Sun, and Y. Lin, "Analyzing urban forest coverage variation in Guangzhou-Foshan region using factorial analysis based multivariate statistical prediction models," *Forest Ecol. Manage.*, vol. 432, pp. 121–131, Jan. 2019.
- [5] J. Degerickx, D. A. Roberts, J. P. McFadden, M. Hermy, and B. Somers, "Urban tree health assessment using airborne hyperspectral and LiDAR imagery," *Int. J. Appl. Earth Observ. Geoinf.*, vol. 73, pp. 26–38, 2018.
- [6] T. Hu, X. Huang, J. Li, and L. Zhang, "A novel co-training approach for urban land cover mapping with unclear Landsat time series imagery," *Remote Sens. Environ.*, vol. 27, pp. 144–157, 2018.
- [7] X. Li, Y. Zhou, Z. Zhu, L. Liang, B. Yu, and W. Cao, "Mapping annual urban dynamics (1985–2015) using time series of Landsat data," *Remote Sens. Environ.*, vol. 216, pp. 674–683, 2018.
- [8] D. Zhou, S. Zhao, L. Zhang, and S. Liu, "Remotely sensed assessment of urbanization effects on vegetation phenology in China's 32 major cities," *Remote Sens. Environ.*, vol. 176, pp. 272–281, 2016.
- [9] Z. Li *et al.*, "Urban landscape extraction and analysis in the mega-city of China's coastal regions using high resolution satellite imagery: A case of Shanghai, China," *Int. J. Appl. Earth Observ. Geoinf.*, vol. 72, pp. 140–150, 2018.
- [10] Y. Xie, Q. Weng, and P. Fu, "Temporal variations of artificial nighttime and their implications for urbanization in the conterminous United States, 2013–2017," *Remote Sens. Environ.*, vol. 225, pp. 160–174, 2019.
- [11] Y. Lu, N. C. Coops, and T. Hermosilla, "Estimating urban vegetation fraction across 25 cities in pan-Pacific using Landsat time series data," *ISPRS J. Photogramm. Remote Sens.*, vol. 126, pp. 11–23, 2017.
- [12] C. Huang, J. Yang, and P. Jiang, "Assessing impacts of urban form on landscape structure of urban green spaces in China using Landsat images based on Google Earth Engine," *Remote Sens.*, vol. 10, no. 10, pp. 1569–1582, Oct. 2018.
- [13] T. Qiu, C. Song, and J. Li, "Impacts of urbanization on vegetation phenology over the past three decades in Shanghai, China," *Remote Sens.*, vol. 9, no. 9, pp. 970–985, Sep. 2017.
- [14] E. B. Wetherley, J. P. McFadden, and D. A. Roberts, "Megacity-scale analysis of urban vegetation temperatures," *Remote Sens. Environ.*, vol. 213, pp. 18–33, 2018.
- [15] C. Small, "Estimation of urban vegetation abundance by spectral mixture analysis," *Int. J. Remote Sens.*, vol. 25, no. 7, pp. 1305–1334, 2010.
- [16] T. R. Tooke, N. C. Coops, N. R. Goodwin, and J. A. Voogt, "Extracting urban vegetation characteristics using spectral mixture analysis and decision tree classifications," *Remote Sens. Environ.*, vol. 113, no. 2, pp. 398–407, 2009.
- [17] M. Rutzinger, B. Höfle, M. Hollaus, and N. Pfeifer, "Object-based point cloud analysis of full-waveform airborne laser scanning data for urban vegetation classification," *Sensors*, vol. 8, no. 8, pp. 4505–4528, 2008.
- [18] J. Tigges, T. Lakes, and P. Hostert, "Urban vegetation classification: Benefits of multitemporal RapidEye satellite data," *Remote Sens. Environ.*, vol. 136, pp. 66–75, 2013.
- [19] X. Zhang, X. Feng, and H. Jiang, "Object-oriented method for urban vegetation mapping using IKONOS imagery," *Int. J. Remote Sens.*, vol. 31, no. 1, pp. 177–196, 2010.
- [20] B. Wang *et al.*, "Assessment of Sentinel-2 MSI spectral band reflectances for estimating fractional vegetation cover," *Remote Sens.*, vol. 10, no. 12, pp. 1927–1946, 2018.
- [21] R. M. Cavalli, L. Fusilli, S. Pascucci, and S. Pignatti, "Hyperspectral sensor data capacity for retrieving complex urban land cover in comparison with multispectral data: Venice City case study (Italy)," *Sensors*, vol. 8, pp. 3299–3320, 2008.
- [22] M. Zribi, S. Le Hégarat-Masclé, O. Taconet, V. Ciarletti, D. Vidal-Madjar, and M. R. Boussemma, "Derivation of wild vegetation cover density in semi-arid regions: Ers2/sar evaluation," *Int. J. Remote Sens.*, vol. 24, no. 6, pp. 1335–1352, 2003.
- [23] K. McGwire, T. Minor, and L. Fenstermaker, "Hyperspectral mixture modeling for quantifying sparse vegetation cover in arid environments," *Remote Sens. Environ.*, vol. 72, pp. 360–374, 2000.
- [24] Y. Ding, H. Zhang, Z. Li, X. Xin, X. Zheng, and K. Zhao, "Comparison of fractional vegetation cover estimations using dimidiate pixel models and look-up table inversions of prosail model from Landsat 8 OLI data," *J. Appl. Remote Sens.*, vol. 10, no. 3, 2016, Art. no. 036022.
- [25] C. Wu, "Normalized spectral mixture analysis for monitoring urban composition using ETM+ imagery," *Remote Sens. Environ.*, vol. 93, pp. 480–492, 2004.
- [26] C. Liao, J. Wang, J. Shang, X. Huang, J. Liu, and T. Huffman, "Sensitivity study of Radarsat-2 polarimetric SAR to crop height and fractional vegetation cover of corn and wheat," *Int. J. Remote Sens.*, vol. 39, no. 5, pp. 1475–1490, 2017.
- [27] X. Wang *et al.*, "Estimating fractional vegetation cover from Landsat 7 ETM+ reflectance data based on a coupled radiative transfer and crop growth model," *IEEE Trans. Geosci. Remote Sens.*, vol. 55, no. 10, pp. 5539–5546, Oct. 2017.
- [28] X. Li, H. Wang, H. Long, D. Wei, and Y. Bao, "A model for the estimation of vegetation cover based on the relationship between vegetation and soil moisture," *Int. J. Remote Sens.*, vol. 33, no. 11, pp. 3580–3595, 2011.
- [29] J. Xiao and A. Moody, "A comparison of methods for estimating fractional green vegetation cover within a desert-to-upland transition zone in central New Mexico, USA," *Remote Sens. Environ.*, vol. 98, pp. 237–250, 2005.
- [30] R. Amiri, Q. Weng, A. Alimohammadi, and S. K. Alavipanah, "Spatial-temporal dynamics of land surface temperature in relation to fractional vegetation cover and land use/cover in the Tabriz urban area, Iran," *Remote Sens. Environ.*, vol. 113, no. 12, pp. 2606–2617, 2009.
- [31] N. B. Mishra, K. A. Grews, and G. S. Okin, "Relating spatial patterns of fractional land cover to savanna vegetation morphology using multiscale remote sensing in the Central Kalahari," *Int. J. Remote Sens.*, vol. 35, no. 6, pp. 2082–2104, 2014.
- [32] F. Priem, A. Okujeni, S. V. D. Linden, and F. Canters, "Comparing map-based and library-based training approaches for urban land-cover fraction mapping from Sentinel-2 imagery," *Int. J. Appl. Earth Observ. Geoinf.*, vol. 78, pp. 295–305, 2019.
- [33] M. J. Lambert, P. G. S. Traoré, X. Blaes, P. Baret, and P. Defourny, "Estimating smallholder crops production at village level from Sentinel-2 time series in Mali's cotton belt," *Remote Sens. Environ.*, vol. 216, pp. 647–657, 2018.
- [34] J. J. Erinjery, M. Singh, and R. Kent, "Mapping and assessment of vegetation types in the tropical rainforests of the Western Ghats using multispectral Sentinel-2 and SAR Sentinel-1 satellite imagery," *Remote Sens. Environ.*, vol. 216, pp. 345–354, 2018.
- [35] M. Sibanda, O. Mutanga, and M. Rouget, "Examining the potential of Sentinel-2 MSI spectral resolution in quantifying above ground biomass across different fertilizer treatments," *ISPRS J. Photogramm. Remote Sens.*, vol. 110, pp. 55–65, 2015.
- [36] R. A. Araya-López, J. Lopatin, F. E. Fassnacht, and H. J. Hernández, "Monitoring Andean high-altitude wetlands in central Chile with seasonal optical data: A comparison between Worldview-2 and Sentinel-2 imagery," *ISPRS J. Photogramm. Remote Sens.*, vol. 145, pp. 213–224, 2018.
- [37] J. G. P. W. Clevers and A. A. Gitelson, "Remote estimation of crop and grass chlorophyll and nitrogen content using red-edge bands on Sentinel-2 and -3," *Int. J. Appl. Earth Observ. Geoinf.*, vol. 23, pp. 344–351, 2013.
- [38] C. Shoko and O. Mutanga, "Examining the strength of the newly-launched Sentinel 2 MSI sensor in detecting and discriminating subtle differences between C3 and C4 grass species," *ISPRS J. Photogramm. Remote Sens.*, vol. 129, pp. 32–40, 2017.
- [39] K. J. Guilfoyle, M. L. G. Althouse, and C. I. Chang, "A quantitative and comparative analysis of linear and nonlinear spectral mixture models using radial basis function neural networks," *IEEE Trans. Geosci. Remote Sens.*, vol. 39, no. 10, pp. 2314–2318, Oct. 2001.
- [40] L. Ma, J. Chen, Y. Zhou, and X. Chen, "Two-step constrained nonlinear spectral mixture analysis method for mitigating the collinearity effect," *IEEE Trans. Geosci. Remote Sens.*, vol. 54, no. 5, pp. 2873–2886, May 2016.
- [41] C. Wu and A. T. Murray, "Estimating impervious surface distribution by spectral mixture analysis," *Remote Sens. Environ.*, vol. 84, pp. 493–505, 2003.
- [42] J. Franke, D. A. Roberts, K. Halligan, and G. Menz, "Hierarchical multiple endmember spectral mixture analysis (MESMA) of hyperspectral imagery for urban environments," *Remote Sens. Environ.*, vol. 113, pp. 1712–1723, 2009.
- [43] B. Somers, G. P. Asner, L. Tits, and P. Coppin, "Endmember variability in spectral mixture analysis: A review," *Remote Sens. Environ.*, vol. 115, pp. 1603–1616, 2011.

- [44] A. M. D. Asis and K. Omasa, "Estimation of vegetation parameter for modeling soil erosion using linear spectral mixture analysis of Landsat ETM data," *ISPRS J. Photogramm. Remote Sens.*, vol. 62, no. 4, pp. 309–324, 2007.
- [45] J. Wang, X. Cao, J. Chen, and X. Jia, "Assessment of multiple scattering in the reflectance of semiarid shrublands," *IEEE Trans. Geosci. Remote Sens.*, vol. 53, no. 9, pp. 4910–4921, Sep. 2015.
- [46] Z. Mitraka, F. D. Frate, and F. Carbone, "Nonlinear spectral unmixing of Landsat imagery for urban surface mapping," *IEEE J. Sel. Topics Appl. Earth Observ. Remote Sens.*, vol. 9, no. 7, pp. 3340–3350, Jul. 2016.
- [47] N. Yokoya, J. Chanussot, and A. Iwasaki, "Nonlinear unmixing of hyperspectral data using semi-nonnegative matrix factorization," *IEEE Trans. Geosci. Remote Sens.*, vol. 52, no. 2, pp. 1430–1437, Feb. 2014.
- [48] T. W. Ray and B. C. Murray, "Nonlinear spectral mixing in desert vegetation," *Remote Sens. Environ.*, vol. 55, pp. 59–64, 1996.
- [49] S. R. Phinn, C. M. Roelfsema, and P. J. Mumby, "Multi-scale, object-based image analysis for mapping geomorphic and ecological zones on coral reefs," *Int. J. Remote Sens.*, vol. 32, no. 12, pp. 3768–3797, 2011.
- [50] C. Zhang, "Multiscale quantification of urban composition from EO-1/Hyperion data using object-based spectral unmixing," *Int. J. Appl. Earth Observ. Geoinf.*, vol. 47, pp. 153–162, 2016.
- [51] D. C. Duro, S. E. Franklin, and M. G. Dubé, "A comparison of pixel-based and object-based image analysis with selected machine learning algorithms for the classification of agricultural landscapes using SPOT-5 HRG imagery," *Remote Sens. Environ.*, vol. 118, pp. 259–272, 2012.
- [52] I. A. Rizvi and B. K. Mohan, "Object-based image analysis of high-resolution satellite images using modified cloud basis function neural network and probabilistic relaxation labeling process," *IEEE Trans. Geosci. Remote Sens.*, vol. 49, no. 12, pp. 4815–4820, Dec. 2011.
- [53] T. Tormos, P. Kosuth, S. Durrieu, S. Dupuy, B. Villeneuve, and J. G. Wasson, "Object-based image analysis for operational fine-scale regional mapping of land cover within river corridors from multispectral imagery and thematic data," *Int. J. Remote Sens.*, vol. 33, no. 14, pp. 4603–4633, 2012.
- [54] M. K. Ridd, "Exploring a V-I-S (vegetation-impervious surface-soil) model for urban ecosystem analysis through remote sensing: Comparative anatomy for cities," *Int. J. Remote Sens.*, vol. 16, no. 12, pp. 2165–2185, 1995.
- [55] J. Luis *et al.*, "Sentinel-2 Sen2cor: L2A processor for users," in *Proc. Living Planet Symp.*, May 2016.
- [56] Trimble eCognition 2018. [Online]. Available: <http://www.ecognition.com/>. Accessed on: Nov. 1, 2018.
- [57] M. D. Hossain and D. Chen, "Segmentation for object-based image analysis (OBIA): A review of algorithms and challenges from remote sensing perspective," *ISPRS J. Photogramm. Remote Sens.*, vol. 150, pp. 115–134, 2019.
- [58] G. Duveiller, F. Baret, and P. Defourny, "Using thermal time and pixel purity for enhancing biophysical variable time series: An interproduct comparison," *IEEE Trans. Geosci. Remote Sens.*, vol. 51, no. 4, pp. 2119–2127, Apr. 2013.
- [59] J. H. Gruninger, A. J. Ratkowski, and M. L. Hoke, "The sequential maximum angle convex cone (SMACC) endmember model," *Proc. SPIE*, vol. 5425, pp. 1–14, 2004.
- [60] J. M. P. Nascimento and J. M. B. Dias, "Vertex component analysis: A fast algorithm to unmixhyperspectral data," *IEEE Trans. Geosci. Remote Sens.*, vol. 43, no. 4, pp. 898–910, Apr. 2005.
- [61] L. Sun, Y. Zhang, and B. Guindon, "Improved iterative error analysis for endmember extraction from hyperspectral imagery," *Proc. SPIE.*, vol. 7086, no. 10, 2008, Art. no. 70860S.
- [62] M. D. Craig, "Minimum-volume transforms for remotely sensed data," *IEEE Trans. Geosci. Remote Sens.*, vol. 32, no. 3, pp. 542–552, May 1994.
- [63] L. Miao and H. Qi, "Endmember extraction from highly mixed data using minimum volume constrained nonnegative matrix factorization," *IEEE Trans. Geosci. Remote Sens.*, vol. 45, no. 3, pp. 765–777, Mar. 2007.
- [64] L. Ma, Y. Zhou, J. Chen, X. Cao, and X. Chen, "Estimation of fractional vegetation cover in semiarid areas by integrating endmember reflectance purification into nonlinear spectral mixture analysis," *IEEE Geosci. Remote Sens. Lett.*, vol. 12, no. 6, pp. 1175–1179, Jun. 2015.
- [65] D. A. Roberts, P. E. Dennison, M. E. Gardner, Y. Hetzel, S. L. Ustin, and C. T. Lee, "Evaluation of the potential of hyperion for fire danger assessment by comparison to the airborne visible/infrared imaging spectrometer," *IEEE Trans. Geosci. Remote Sens.*, vol. 41, no. 6, pp. 1297–1310, Jun. 2003.
- [66] F. D. V. D. Meer and X. Jia, "Collinearity and orthogonality of endmember in linear spectral unmixing," *Int. J. Appl. Earth Observ. Geoinf.*, vol. 18, pp. 494–503, 2012.
- [67] X. Chen, J. Chen, X. Jia, B. Somers, J. Wu, and P. Coppin, "A quantitative analysis of virtual endmembers' increased impact on the collinearity effect in spectral Unmixing," *IEEE Trans. Geosci. Remote Sens.*, vol. 49, no. 8, pp. 2945–2956, Aug. 2011.
- [68] A. J. Elmore, J. F. Mustard, S. J. Manning, and D. B. Lobell, "Quantifying vegetation change in semiarid environments: Precision and accuracy of spectral mixture analysis and the normalized difference vegetation index," *Remote Sens. Environ.*, vol. 73, no. 1, pp. 87–102, 2000.



Yaotong Cai received the B.S. degree in forestry from the Central South University of Forestry and Technology (CSUFT), Changsha, China, in 2018, where he is currently working toward the master's degree in forestry remote sensing.

His research interests include image classification and biomass estimation.



Meng Zhang received the M.S. degree in geography from Hunan Normal University, Changsha, China, in 2010, and the Ph.D. degree in cartography and geographic information engineering from Central South University, Changsha, China, in 2014.

He is currently a Teacher with the College of Forestry, Central South University of Forestry and Technology, Changsha, China. He has authored more than 15 research papers indexed by SCI and EI. His research interests include resources and environment remote sensing and GIS.



Hui Lin received the B.S., M.S., and Ph.D. degrees in forest management from the Central South University of Forestry and Technology, Changsha, China, in 1988, 1991, and 2005.

She is a Professor with the College of Forestry, Central South University of Forestry and Technology, Changsha, China. She has authored more than 170 research papers published in which 30 papers indexed by SCI. Her research interests include forest remote sensing and GIS.